Volcanic satellites tidally venting Na, K, SO_2 in optical & infrared light

Oza, A.V.; Gebek, A.; Westram, M.M. zu .; Tokadjian, A.; Piro, A.L.; Hu, R.; … ; Lopes, R.M.C.

Monthly Notices of the ROYAL ASTRONOMICAL SOCIETY

MNRAS **546,** 1–10 (2026) https://doi.org/10.1093/mnras/staf1526
Advance Access publication 2025 September 25

Volcanic satellites tidally venting Na, K, and SO_2 in optical and infrared light

Apurva V. Oza ,[1,2★] Andrea Gebek ,[3] Moritz Meyer zu Westram,[4] Armen Tokadjian,[2] Anthony L. Piro,[5] Renyu Hu,[1,2] Athira Unni ,[6] Raghav Chari,[7] Aaron Bello-Arufe,[2] Carl A. Schmidt,[8] Amy J. Louca ,[9] Yamila Miguel,[9,10] Raissa Estrela,[2] Jeehyun Yang,[2] Mario Damiano,[2] Yasuhiro Hasegawa,[2] Luis Welbanks ,[11] Diana Powell,[12] Rishabh Garg,[13] Pulkit Gupta,[14] Yuk L. Yung[1] and Rosaly M. C. Lopes[2]

[1]*Division of Geological and Planetary Sciences, California Institute of Technology, Pasadena, CA 91125, USA*
[2]*Jet Propulsion Laboratory, California Institute of Technology, Pasadena, CA 91109, USA*
[3]*Sterrenkundig Observatorium, Universiteit Gent, B-9000 Gent, Belgium*
[4]*Physikalisches Institut, Universität Bern, Ch-3012 Bern, Switzerland*
[5]*The Observatories of the Carnegie Institution for Science, Pasadena, CA 91101, USA*
[6]*Department of Astronomy & Astrophysics, University of California, Santa Cruz, CA 95064, USA*
[7]*New York University, New York, NY 10003, USA*
[8]*Center for Space Physics, Boston University, Boston, MA 02215, USA*
[9]*Leiden Observatory, Leiden University, NL-2311 GW Leiden, the Netherlands*
[10]*SRON Netherlands Institute for Space Research, NL-2333 CA Leiden, the Netherlands*
[11]*School of Earth and Space Exploration, Arizona State University, Tempe, AZ 85281, USA*
[12]*Department of Astronomy & Astrophysics, University of Chicago, Chicago, IL 60637, USA*
[13]*Portola High School, Irvine, CA 92618, USA*
[14]*Indian Institute of Technology, Indore, Madhya Pradesh 453552, India*

Accepted 2025 August 4. Received 2025 August 3; in original form 2025 January 3

ABSTRACT

Recent infrared spectroscopy from the *James Webb Space Telescope* (*JWST*) has spurred analyses of common volcanic gases such as carbon dioxide (CO_2), sulphur dioxide (SO_2), alongside alkali metals sodium (Na I) and potassium (K I) surrounding the hot Saturn WASP-39 b. We report more than an order-of-magnitude of variability in the density of neutral Na, K, and SO_2 between ground-based measurements and *JWST*, at distinct epochs, hinting at exogenic physical processes similar to those sourcing Io's extended atmosphere and torus. Tidally heated volcanic satellite simulations sputtering gas into a cloud or toroid orbiting the planet are able to reproduce the probed line-of-sight column density variations. The estimated SO_2 flux is consistent with tidal gravitation predictions, with a Na/SO_2 ratio far smaller than Io's. Although stable satellite orbits at this system are known to be $<$15.3 h, several high-resolution alkali Doppler shift observations are required to constrain a putative orbit. Due to the Roche limit interior to the planetary photosphere at $\sim$8 h, atmosphere–exosphere interactions are expected to be especially important in this system.

Key words: planets and satellites: atmospheres – planets and satellites: detection – planets and satellites: dynamical evolution and stability – planets and satellites: physical evolution – planets and satellites: rings.

1 INTRODUCTION

At the time of this writing, Saturn has 274 confirmed moons in orbit; 210 were discovered in the past decade alone (S. S. Sheppard et al. 2018, 2023), 128 of which were reported while this paper was in revision by the Minor Planet Center on 2025 March 11, following an irregular satellite campaign at the Canada–France–Hawaii Telescope (E. Ashton et al. 2025). It is now well known that Saturn's rings are actively shaped by its natural satellites (S. Charnoz et al. 2018). Another splendid example is Enceladus, which actively shapes Saturn's E-ring due to its tidally heated hydrothermal venting, leading to a hydroxide torus of gas (R. E. Johnson et al. 2006a) and grains. Of course, Io is well known to host a micron bar volcanic and sublimated sulphur dioxide SO_2 atmosphere observed to vary from 10^{16} to 10^{17} SO_2 cm^{-2} (E. Lellouch et al. 2015). In fact, SO_2 is one of the most common gases, along with CO_2 and H_2O, released in a volcanic eruption on Earth. Ongoing volcanism on Venus was only recently confirmed (R. R. Herrick & S. Hensley 2023; D. Sulcanese, G. Mitri & M. Mastrogiuseppe 2024) despite its obvious atmospheric SO_2 signature with *Venus express* measurements at 0.02 ppm below 90 km and roughly 5 ppm above 100 km (A. Mahieux et al. 2023). In

★ E-mail: oza@caltech.edu

terms of discovered elements at exoplanets, the relative abundances of volatile metals, notably neutral sodium (Na I), potassium (K I), and SO_2 are well known to be sensitive to silicate lava temperatures (B. Fegley & M. Y. Zolotov 2000), reminding us of one of their origins as silicate magmas.

In principle, if a third body were to be present at a planetary system, the natural satellite would experience tidal heating should it be in a perturbed or eccentric orbit (S. J. Peale, P. Cassen & R. T. Reynolds 1979).

Especially exciting is the case for a habitable-zone exomoon (A. Tokadjian & A. L. Piro 2023), possibly outshining the planet itself from 6 to 8 μm in the infrared (IR), due to the satellite blackbody flux being boosted by tidal heating.

Novel techniques to detect IR-bright exomoons in spectroscopy (e.g. E. Kleisioti et al. 2023, 2024) has spawned multiwavelength searches in radio (M. Narang et al. 2023a, b) and thanks to the bright sodium and potassium lines in absorption spectroscopy, visible light (A. V. Oza et al. 2019). At transiting exoplanet systems, putative exomoons are subject not only to the host planet's gravitational tide, but also the massive gravitational field of the host star. Beyond a planetary orbit of a couple days, tides dissipate energy into the interior of the satellite due to orbital resonance, rather than decay its orbit (T. A. Cassidy et al. 2009, see also Fig. 5). The tidal field of the star and planet in concert, acting on a natural satellite, drives three-body gravitational heating, an expression derived in T. A. Cassidy et al. (2009) and A. V. Oza et al. (2019), which is far larger at a close-in system than canonical eccentricity-driven tides (S. J. Peale et al. 1979). Three-body heating is so large that gas and grain volcanism on these putative satellites is inevitable and predicted to be roughly $\sim 10^{5\pm1}$ times the energy measured at Io (G. J. Veeder et al. 1994). As a first approximation, if the satellite has an unknown size $R_{☽} \sim R_{\rm Io}$, orbiting a Jupiter or Saturn-sized object over a range of orbital periods $2 \lesssim \tau_{\rm p} \lesssim 5$ d (equilibrium temperatures of $\sim 1000 \lesssim T_{\rm eq} \lesssim 2500$ K), the tidal venting rate computed by A. V. Oza et al. (2019) is roughly $\approx 10^{8\pm1}$ kg s^{-1} (more than 100× Io's). Of course, depending on the size and magmatic state of putative rocky exomoons, thermal evaporation may also source $\dot{M} \gg 10^8$ kg s^{-1} (A. V. Oza et al. 2019). Whether this range of volcanism is observable, and whether any of these putative exomoons have survived disintegration, leads us to the current investigation of IR data with *James Webb Space Telescope* (*JWST*) mid-infrared (MIR) and near-infrared (NIR) data.

We focus on one of the farthest host planets from the sample of extrasolar-Ios studied by A. V. Oza et al. (2019) at $\tau_{\rm p} \sim 4.1$ d. The distance allows for a larger Hill sphere where natural satellites are dynamically stable (A. M. Kisare & D. C. Fabrycky 2024). WASP-39 b is a highly inflated hot Saturn orbiting a $m_{\rm K} = 12.11$, G7 host star located 215.4 ± 0.7 pc away (F. Faedi et al. 2011). Fortunately, WASP-39 b has been heavily monitored in visible light (by the *Hubble Space Telescope*/Space Telescope Imaging Spectrograph (*HST*/STIS; P. D. Fischer et al. 2016; D. K. Sing et al. 2016), Very Large Telescope (VLT)/FOcal Reducer and low dispersion Spectrograph 2 (FORS2; N. Nikolov et al. 2016)), and by *JWST* in the NIR (H. R. Wakeford et al. 2018; E.-M. Ahrer et al. 2023; L. Alderson et al. 2023; A. D. Feinstein et al. 2023; Z. Rustamkulov et al. 2023), and MIR (D. Powell et al. 2024) for 11 total epochs. In this short letter, we provide a volcanic alternative to the robust H_2S-driven atmospheric photochemistry (Y. L. Yung & W. B. Demore 1999; S.-M. Tsai et al. 2023; J. Yang & R. Hu 2024) as a source for SO_2. In this light, we determine the optically thin Na I, CO_2, and SO_2 column densities from available data using the technique of evaporative transmission spectroscopy (A. Gebek & A. V. Oza 2020) in Section 2. Lastly, as a test case in Section 3, we simulate the toroidal exosphere of WASP-39 b sourced by an outgassing rate $\dot{M}$ via the exomoon torus software: DISHOOM and SERPENS (M. Meyer zu Westram et al. 2024). Finally, we discuss implications and future outlook in Section 4.

2 EVAPORATIVE TRANSMISSION SPECTRA ANALYSIS

We first consider simplistic optically thin absorption from atoms and molecules in a tenuous exosphere. In this optically thin scenario, the transit depth is directly proportional to the number of absorbing particles spread over the stellar disc, expressed as the change in stellar flux over a wavelength region λ (B. T. Draine 2011; A. Gebek & A. V. Oza 2020):

$$\frac{dF_\lambda}{F_\star} \approx N\sigma(\lambda), \quad (1)$$

where $\sigma(\lambda)$ is the absorption cross-section, and N (cm^{-2}) the average line-of-sight (LOS) column density of the absorber. Fig. 1 shows how the transit depth $dF_\lambda/F_\star$ near the alkali absorption lines varies between epochs (black, blue, and red data points).

As described more in Section 3, the total number of absorbing particles can be estimated by a mass-loss relation:

$$\mathcal{N} = (\dot{M}/m)\,\tau_\gamma, \quad (2)$$

where m is the volatile mass, τ_γ is the lifetime against photoionization, approximating a *cloud* of particles limited by the ambient solar field. More generally, τ_γ can be described for an arbitrary species τ_i and physical processes (A. V. Oza et al. 2019).[1] To approximate a *toroid*, we adopt the value $\tau_{\rm tor} \sim 3$ h by M. Meyer zu Westram (2023) characteristic of charge-exchange (R. E. Johnson & D. F. Strobel 1982) and other well-known processes at Jupiter-Io plasma torus (C. Schmidt et al. 2023). In this way $\dot{M}_\gamma$ and $\dot{M}_{\rm tor}$ are inferred mass-loss rates to power the observed LOS column densities $\bar{N} \sim \mathcal{N}/(\pi R_\star^2)$, so that the column density is directly proportional to the mass-loss rate:

$$N \sim \dot{M}\frac{\tau_i}{m_i \pi R_\star^2}, \quad (3)$$

where $\mathcal{N}$ (equation 2) can be distributed into a photoionized cloud or plasma torus geometry (A. Gebek & A. V. Oza 2020).

Table 2 shows (a) for atomic features, the computed column densities (equation 1) for each epoch of data and equivalent widths (see Section 2.1); (b) for molecular features, column densities and temperatures (Section 2.2); and (c) mass-loss rates for both atoms and molecules (as described by equations 2 and 3).

2.1 Alkali gas in the optical

One can approximate N of neutral sodium and potassium analytically by the sum of two Voigt profiles (approximating the D2 and D1 alkali resonance lines). As the low-resolution data here do not resolve these absorption lines, we measured the equivalent width (W_λ) of the line relative to the continuum determined by the normalization fit to the data near the Na and K resonance lines. W_λ therefore is directly proportional to N, given by B. T. Draine (2011):

$$W_\lambda = \frac{\pi e^2}{m_e c^2}(f_{\rm D2}\lambda_{\rm D2}^2 + f_{\rm D1}\lambda_{\rm D1}^2) \times N, \quad (4)$$

[1] $\tau_{\gamma,{\rm CO_2}} = 2.3$ h; $\tau_{\gamma,{\rm SO_2}} = 2.5$ m; $\tau_{\gamma,{\rm Na}} = 6.6$ m; $\tau_{\gamma,{\rm K}} = 1.8$ m.

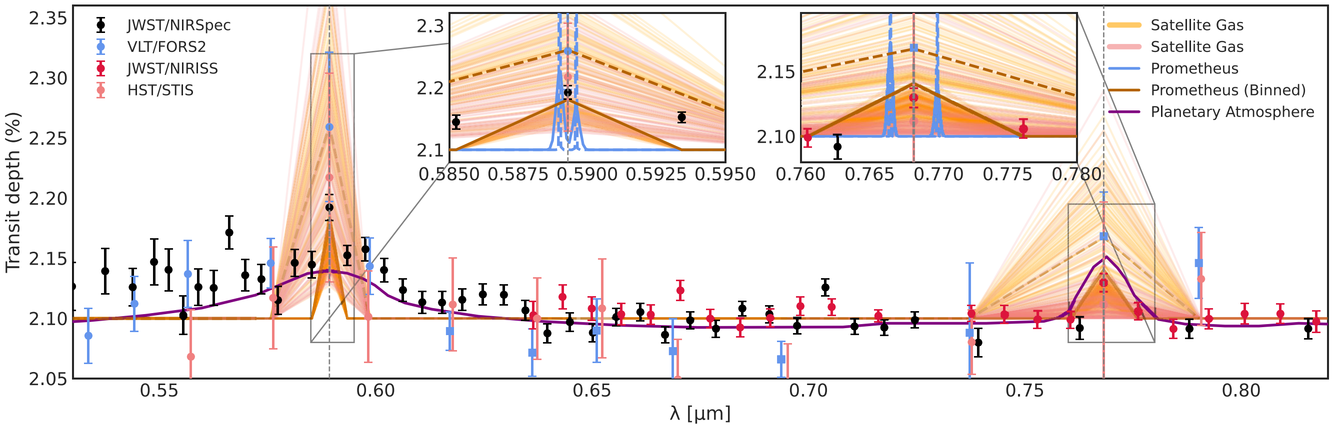

Figure 1. Alkali metals: Na I and K I as observed by the VLT (blue) (N. Nikolov et al. 2016), *HST* (pink) (P. D. Fischer et al. 2016), *JWST*/NIRISS (red) (A. D. Feinstein et al. 2023), and *JWST*/NIRSpec (black) (Z. Rustamkulov et al. 2023), with accompanying planetary (1D radiative–convective–thermochemical equilibrium: purple) and satellite gas (orange for VLT and *JWST*, pink for *HST*) simulated with 100 optically thin models cf. equation (1) approximating equivalent widths $W_\lambda \propto N$ (equation 4) reported in Table 2. Zoom inset: PROMETHEUS forward models are shown in high resolution (satellite cloud: blue-dashed; torus: blue solid) and binned to the data (brown in the respective line styles).

where e is the elementary charge, $m_{\rm e}$ is the electron mass, c is the speed of light, and $f_{\rm D}$ ($\lambda_{\rm D}$) is the oscillator strength (wavelength) of the D-line alkali transition, as also summarized in A. V. Oza et al. (2019, equation 14). This is an approximation as discussed by B. T. Draine (2011) is exact for $\tau_0 \to 0$, and within 2.6 per cent for the optically thin $\tau_0 < 1.256$, in the limit where the term $(1/(1 + (\tau_0/2\sqrt(2))))$ approaches unity. It follows that the measured equivalent width of the sodium and potassium lines is directly related to the average LOS column density N, reducing to the number of absorbing atoms $\mathcal{N} \sim N\pi R_\star^2$ (R. E. Johnson & P. J. Huggins 2006) modelled in 3D in Section 3. For each individual transit of WASP-39 b, neutral sodium and potassium column densities are simulated with 100 optically thin models following equation (1) indicated in orange and pink corresponding to the data sets identified in the caption, approximating the range of column densities derived from their equivalent widths following equation (4) (B. T. Draine 2011), reported in Table 2. PROMETHEUS simulations (A. Gebek & A. V. Oza 2020) (indicated in blue, brown (binned)) approximate gas density minima values provided in Table 1.

In Fig. 1, we employ the radiative transfer tool PROMETHEUS to model the transit depth of a satellite gas source following A. Gebek & A. V. Oza (2020), distributing a packet of evaporating $\mathcal{N}$ particles into two distinct geometries: (1) toroid (solid blue) and (2) sputtered cloud (dashed blue). Due to the tenuous nature and limited extent of the cloud scenario, the dashed absorption lines are narrow, probing mostly the line core. The planetary atmosphere (purple) is adopted from Z. Rustamkulov et al. (2023) assuming chemical equilibrium in a hydrostatic atmosphere. The simulated minimum alkali column densities are computed here from equation (4) (Table 2) based on the sodium and potassium data seen by VLT, *HST*, and *JWST*. Strikingly, the data are not consistent within error. Moreover, we find that the equivalent width changes by a factor of 7.4 from epoch to epoch for sodium, and more than 1.3 to a surprising disappearance for potassium. Two PROMETHEUS models are shown in Fig. 1: (1) an alkali toroid (solid blue) with a semimajor axis, $a_{\rm torus} \sim 1.5\ R_{\rm p}$ and 1D velocity dispersion $\sigma_v \sim 62.7\ {\rm km\,s^{-1}}$, which if due to thermal motions, described in A. Gebek & A. V. Oza (2020) equation (2) as a line temperature, follows a Maxwell Boltzmann distribution with average velocity: $\bar{v}_{\rm MB} = \sqrt{8k_{\rm b}T/\pi m}$ (F. Reif 1965) so that

$$v_{\rm kin} = \sqrt{\frac{8}{\pi}}\sigma_v \quad (5)$$

roughly 100 km s^{-1}, characteristic of energetic neutral atoms and plasma interactions at Jupiter-Io (J. K. Wilson et al. 2002; M. Meyer zu Westram 2023). Secondly, (2) an alkali cloud (dashed blue) orbiting at 0.41 $R_{\rm Hill}$ (A. M. Kisare & D. C. Fabrycky 2024) fuelled by an exomoon at $a_{☽} \sim 1.5\ R_{\rm p}$ on a $\tau_{☽} \approx 15.3$ h orbit (cf. Table 1).

Specifically, a satellite cloud (dashed orange PROMETHEUS line in Fig. 1) with a column density of $\sim 10^{11.45}$ Na cm^{-2} roughly approximates the observed VLT (blue) and *HST* (pink) absorption values: ($\sim 10^{11.65}$ and $\sim 10^{11.60}$ cm^{-2}, respectively), whereas the *JWST*/NIRSpec (black) epoch is slightly more tenuous $\sim 10^{10.78}$ cm^{-2}, roughly consistent with a torus (solid, orange PROMETHEUS line in Fig. 1) fuelled by $\sim 7.2 \times 10^{32}$ Na I particles. In the *JWST*/NIRISS data set (red), the potassium column is $\sim 10^{10.61}$ cm^{-2}, which PROMETHEUS simulations approximate with $\sim 3 \times 10^{32}$ K I particles in a toroidal geometry. Although high-resolution observations are needed to quantify Na and K variability distinct from a superstellar planetary atmosphere (D. Powell et al. 2024), the variability in K I is particularly stark, with detections in the VLT and *JWST*/NIRISS epochs ($\sim 10^{11.4}$–$10^{10.6}$ cm^{-2}) contrasted by a disappearance in the *JWST*/NIRSpec and *HST* epochs (Table 2), which may be suggestive of an orbiting satellite cloud $\sim 10^{12.1}$ cm^{-2}, varying its phase along the observer's LOS (M. Meyer zu Westram 2023).

2.2 Volcanic gas in the infrared

For molecular absorption in the NIR and MIR, the approximation in equation (4) is more complex, as σ_λ is no longer an analytical function of wavelength, but rather a composite of many line transitions. We therefore model the observed SO_2 and CO_2 NIR and MIR transit depth $dF_\lambda/F_\star$ in the optically thin limit (equation 1) by computing $\sigma(\lambda)$ on a T–P grid from the ExoMOL data base (J. Tennyson et al. 2024) in order to infer N and its error. Assigning a temperature and a pressure to the gas is a significant simplification of the problem, as the upper atmosphere or exosphere is generally not in local

Table 1. Optically thin alkali column density minima N, corresponding 1D velocity dispersions σ_v, and approximate kinetic velocities (equation 5) for MCMC posterior simulations (top; orange in Fig. 1) and PROMETHEUS models (bottom; blue, brown). Transit depths are normalized at $c = 0.0210$. Satellite cloud and tori geometries are indicated as (☽) and (torus), respectively.

Telescope (alkali) Instrument	VLT (Na) FORS2	*HST* (Na) STIS	*JWST* (Na) NIRSpec	VLT (K) FORS2	*HST* (K) STIS	*JWST* (K) NIRISS	*JWST* (K) NIRSpec
Epoch	2016-3-8	2013-3-17	2022-7-10	2016-3-12	2013-3-17	2022-7-27	2022-7-10
$dF_\lambda/F_\star$ (per cent)	$2.234^{+0.067}_{-0.067}$	$2.189^{+0.078}_{-0.050}$	$2.190^{+0.011}_{-0.011}$	$2.143^{+0.042}_{-0.039}$	$2.095^{+0.040}_{-0.021}$	$2.127^{+0.008}_{-0.008}$	$2.125^{+0.001}_{-0.001}$
$\log N$ (cm^{-2}) MCMC	$11.76^{+0.18}_{-0.28}$	$11.54^{+0.27}_{-0.33}$	$10.96^{+0.43}_{-0.10}$	$11.46^{+0.26}_{-0.61}$	$10.94^{+0.62}_{-0.63}$	$10.62^{+0.19}_{-0.17}$	$9.96^{+1.36}_{-1.36}$
σ_v (km s^{-1})	$31.6^{+116.3}_{-25.2}$	$32.4^{+119.0}_{-25.8}$	$89.1^{+124.7}_{-50.2}$	$28.8^{+112.4}_{-22.5}$	$30.2^{+117.7}_{-23.9}$	$11.5^{+39.8}_{-9.1}$	$0.98^{+1.16}_{-0.52}$
$v_{\rm kin}$ (km s^{-1})	50.5	51.6	142.2	46.0	48.2	18.3	1.56
$\log N$ (cm^{-2}) PROMETHEUS	11.45 (☽)	–	10.77 (torus)	11 (☽)	–	10.38 (torus)	–
σ_v (km s^{-1})	7.8	–	62.7	7.8	–	62.7	–
$v_{\rm kin}$ (km s^{-1})	12.5	–	100	12.5	–	100	–

Table 2. Optically thin column densities for various volcanic species. For atoms, we report the equivalent width (W_λ) in mÅ, and for molecules, we report the temperature $T_{\rm kin}$ in K. NIR retrievals are from 3.9 to 4.5 μm, MIR retrievals from 6 to 8 μm. Normalizations: *JWST*/PRISM $2.107^{+0.006}_{-0.007}$; *JWST*/G395H $2.089^{+0.006}_{-0.006}$; and *JWST*/MIRI $2.108^{+0.007}_{-0.007}$. Column densities N are estimated by transit depths as described for atoms via W_λ in Section 2.1, and inverse models for molecules in Section 2.2. $\dot{M}$ represents the inferred mass-loss rates. γ- and torus-limited describe photoionization-limited clouds and tori with ~3 h charge-exchange lifetimes.

Epoch	Atom	Instrument	N (cm^{-2})	W_λ (mÅ)	$\dot{M}_{\rm tor}$–$\dot{M}_\gamma$ (kg s^{-1})
2016-03-08	Na	VLT/FORS2	$10^{11.65^{+0.19}_{-0.36}}$	131 ± 73	(0.8–81) × 10^5
2013-03-17	Na	*HST*/STIS/G750L	$10^{11.60^{+0.27}_{-0.81}}$	119 ± 109	(0.3–87) × 10^5
2022-07-10	Na	*JWST*/NIRSpec	$10^{10.78^{+0.11}_{-0.15}}$	17.8 ± 5.2	(0.2–9.1) × 10^4
2016-03-12	K	VLT/FORS2	$10^{11.42^{+0.29}_{-1.43}}$	136 ± 131	(0.7–380) × 10^5
2013-03-17	K	*HST*/STIS/G750L	$<10^{10.43}$	14.0 ± 233.6	<35 × 10^5
2022-07-10	K	*JWST*/NIRSpec	$<10^{10.47}$	15.5 ± 28.7	<6.2 × 10^5
2022-07-27	K	*JWST*/NIRISS	$10^{10.61^{+0.12}_{-0.17}}$	21.3 ± 7.0	(0.2–39) × 10^5
Epoch	Molecule	Instrument	N (cm^{-2})	$T_{\rm kin}$ (K)	$\dot{M}_{\rm tor}$–$\dot{M}_\gamma$ (kg s^{-1})
2022-07-30	SO_2	*JWST*/G395H	$10^{16.7^{+0.1}_{-0.1}}$	1100^{+120}_{-110}	(0.6–40) × 10^{11}
2022-07-10	SO_2	*JWST*/NIRSpec	$10^{16.4^{+0.2}_{-0.5}}$	780^{+460}_{-330}	(0.3–20) × 10^{11}
2023-02-14	SO_2	*JWST*/MIRI	$10^{15.1^{+0.2}_{-0.5}}$	1180^{+1400}_{-690}	(0.15–10) × 10^{10}
2022-07-30	CO_2	*JWST*/G395H	$10^{15.46^{+0.03}_{-0.03}}$	2200^{+140}_{-100}	(2.4–3.0) × 10^8
2022-07-10	CO_2	*JWST*/NIRSpec	$10^{15.44^{+0.02}_{-0.02}}$	2000^{+70}_{-90}	(2.3–2.9) × 10^8

thermodynamical equilibrium, well known for Io's MIR SO_2 bands (E. Lellouch et al. 2015). Here, we assume the lowest tabulated pressure value of 0.1 nbar when extracting ExoMOL opacities. We find that increasing pressure up to 0.1 μbar hardly affects the molecular opacities considered here, and are therefore representative of minima. We leave temperature as a free parameter from $T = 100$–3400 K and allow each absorbing species to have a different T. Additionally, we assume a constant normalization, treated as a free parameter. Overall, this leaves us with two free parameters for each absorber contributing to the observed transit depth, plus one free parameter regulating the normalization. We use flat priors for T, $\log_{10}(N/\text{cm}^{-2})$, and $\log_{10}(\sigma_v/(\text{km s}^{-1}))$. We run a PYTHON Markov chain Monte Carlo (MCMC) EMCEE sampler (D. Foreman-Mackey et al. 2013) with 32 walkers for 5000 steps, and discard the first 1000 steps as burn-in. The results (column densities and temperatures) from the optically thin retrieval for the various IR data sets are summarized in Table 2 for molecules, with the accompanying spectra and posterior distributions in Fig. 2. Whereas an extended atmosphere of WASP-39 b is expected to return a consistent signal across planetary transit epochs, an exomoon orbit naturally leads to order-of-magnitude changes in column density and, consequently, spectral transit depth. For instance the SO_2 flux from the 2022-07-30 epoch to 2023-02-14 has varied from $N_{SO_2} \sim 10^{16.7\pm0.1}$ to $N_{SO_2} \sim 10^{15.1^{0.2}_{-0.5}}$ SO_2 cm^{-2}, far larger than the CO_2 variability. Indeed, the CO_2 appears to be consistent despite the optically thin approximation on average near $\sim 10^{15.45\pm0.03}$ CO_2 cm^{-2}, implying the SO_2 is indeed suggestive. Although, WASP-39 has not been reported to be active (F. Faedi et al. 2011), 2/14 exomoon candidates from the A. V. Oza et al. (2019) sample, highlight sources of variability worth considering. Starspots crossings at WASP-52 were shown to modulate H_2O abundances (M. Fournier-Tondreau et al. 2025), while at WASP-31 b puzzling detections and non-detections of K I by the VLT in both low- and high-resolution spectroscopy were reported to be instrumental, albeit with no systematic identified (N. P. Gibson et al. 2019). Multi-epoch observations with the same instrument are therefore essential to characterize variability. Indeed at the volcanic exoplanet candidate, 55 Cancri e (L. C. Quick et al. 2020), toroidal behaviour near 4 μm is seen across multiple epochs with the same

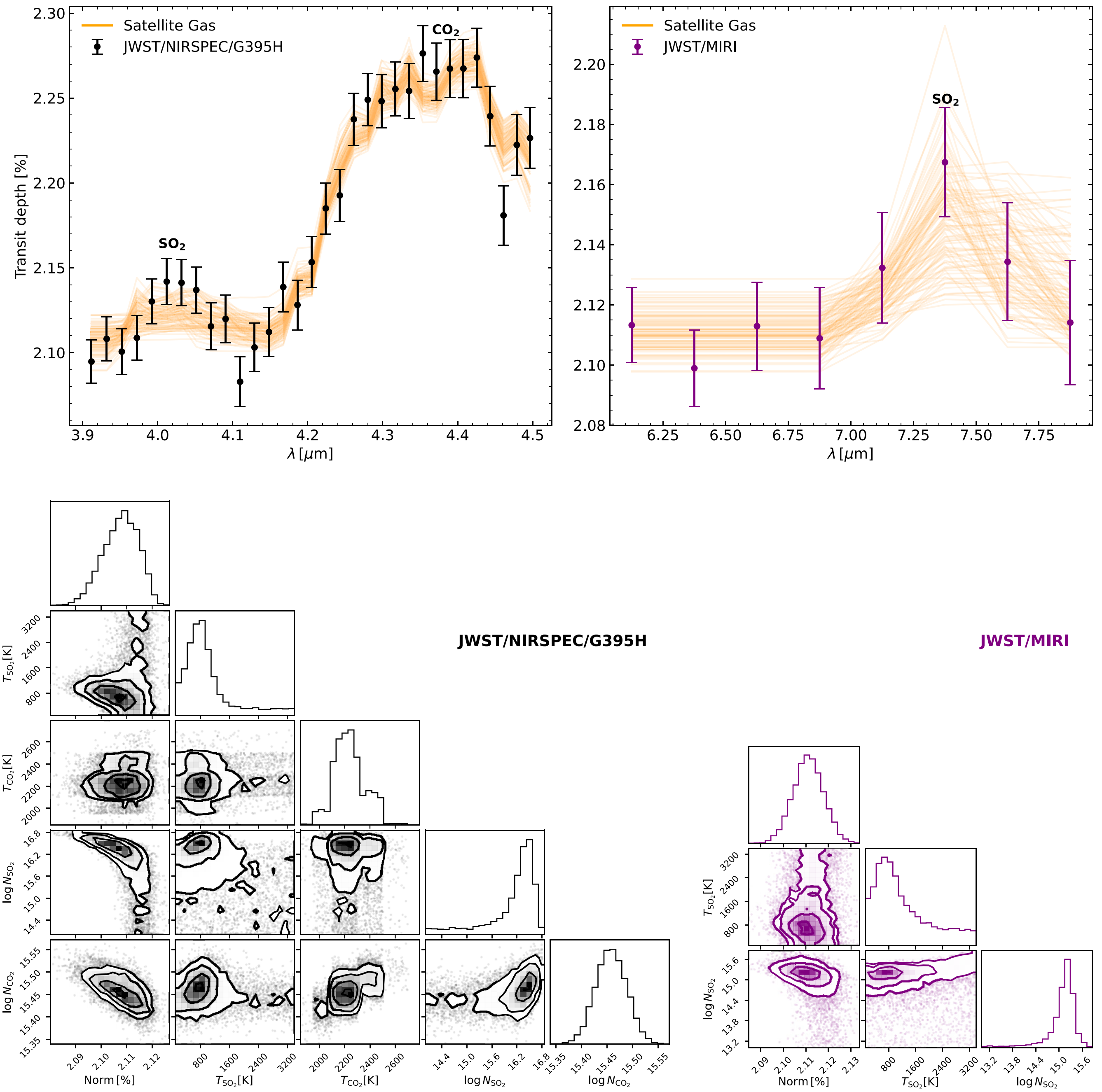

Figure 2. Top panels: 100 optically thin transmission spectra models of SO_2 and CO_2 gas in orange, with central values listed in Table 2. Bottom panels: Posterior distributions, including the temperature T of the gas, column density N, and normalization. *JWST* NIR data are in black and MIR in purple.

JWST instrument (J. A. Patel et al. 2024). We now use the optically thin analytic and PROMETHEUS forward models as a benchmark for detailed Na, K, and SO_2 3D Monte Carlo simulations of the approximate toroidal gas geometry in the next section.

3 NUMERICAL ESTIMATES OF VOLCANIC GAS DENSITIES

In addition to fitting the NIR and MIR observations as described in Section 2, we employ the test-particle Monte Carlo code SERPENS (M. Meyer zu Westram 2023; M. Meyer zu Westram et al. 2024) for first-order simulation analysis in Fig. 3. We infer Na, K, and SO_2 particle and LOS densities at regular time intervals from the WASP-39 b system, which is simulated with the inclusion of a putative exomoon WASP-39 b I as the particle source. We distinguish between a cloud and toroidal scenario as described in Section 2 on evaporative transmission spectroscopy analysis, where the density computations are normalized by maintaining a constant total number of atoms $\mathcal{N}$ of mass m in the simulation, following the analytical approximation in equation (2).

Considering the proximity of the star, we incorporate radiation pressure forces following the methodology outlined in M. Meyer zu Westram et al. (2024). We primarily consider $R_{☽} \sim R_{\mathrm{Io}}$, although a terrestrial-sized volcanic satellite (e.g. A. Bello-Arufe et al. 2025)

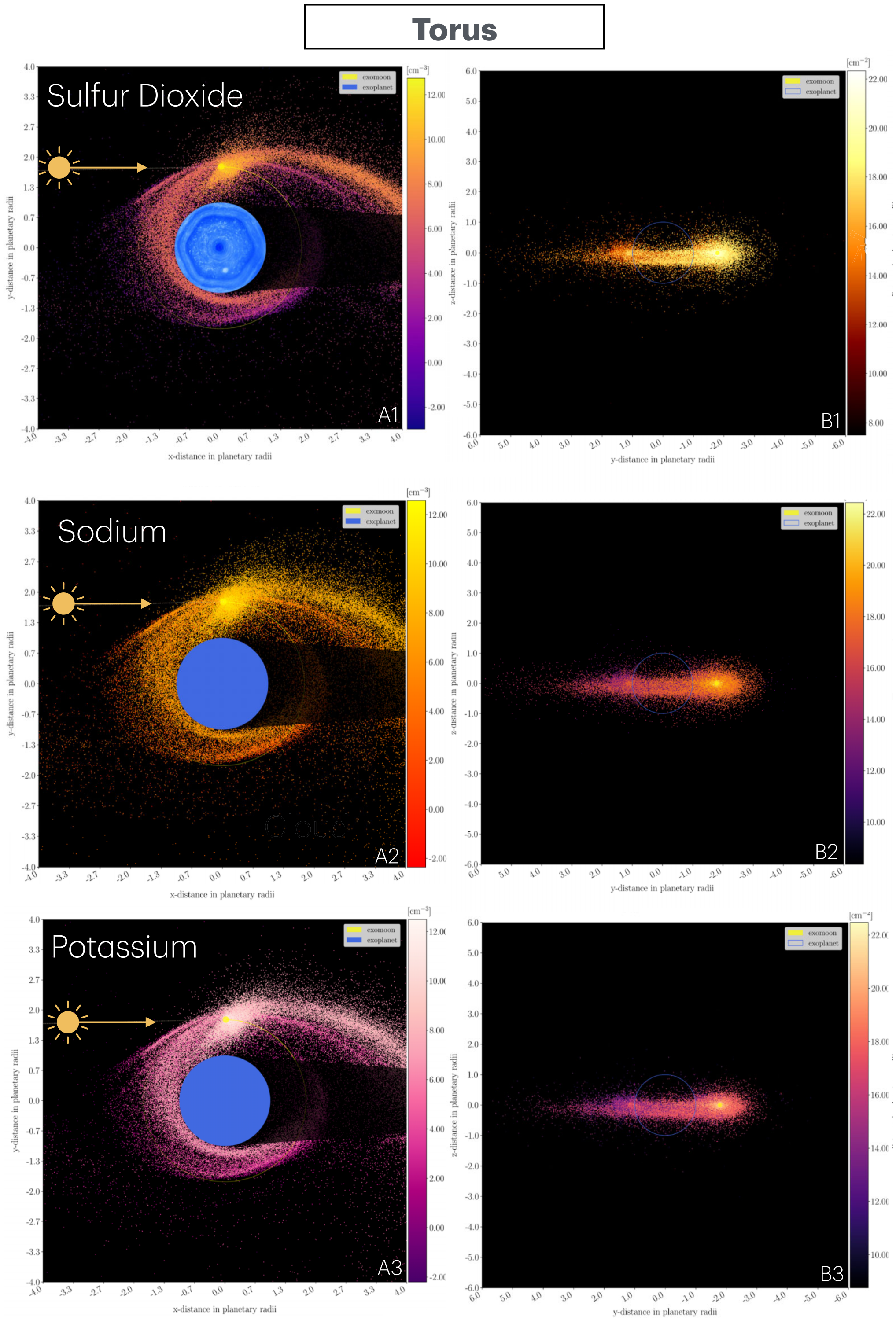

(a)

Figure 3. (a) SERPENS Monte Carlo simulations of neutral SO_2, Na, and K around an *exo-Io* for a toroidal geometry. Top down (first column: A1, A2, and A3) and LOS (second column: B1, B2, and B3) simulations. The approximate total number of particles reproducing the evaporative transmission spectra simulated by PROMETHEUS in Section 2 is $\mathcal{N}_{\rm Na} = 10^{32.82}$, $\mathcal{N}_{\rm K} = 10^{32.97}$, and $\mathcal{N}_{\rm SO_2} = 10^{39}$ atoms/molecules in the system. Particles inside the exoplanet shadow have a lifetime of 3 h for all cases.

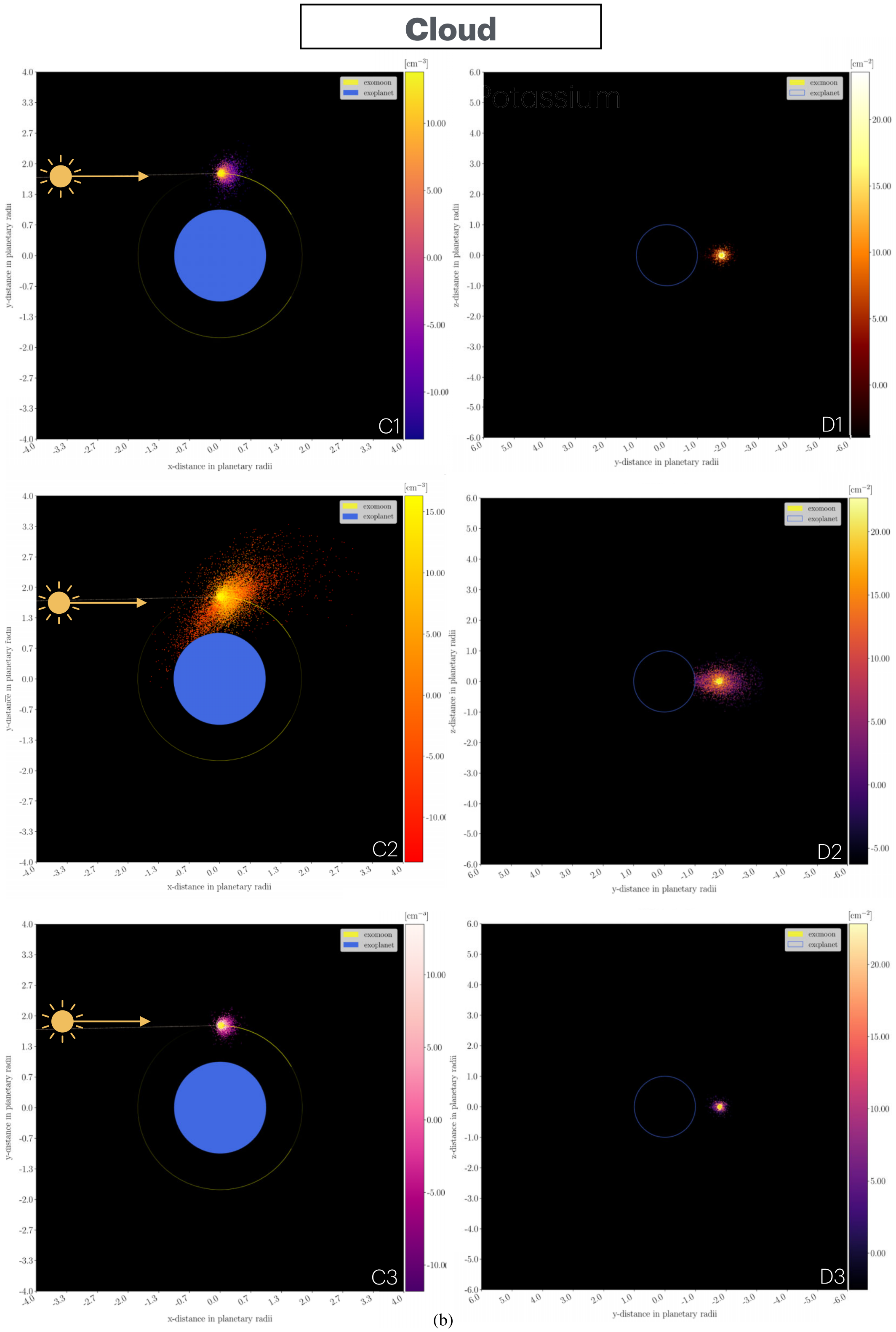

(b)

Figure 3. (b) Cloud geometry. Top down (first column: C1, C2, and C3) and LOS: (second column: D1, D2, and D3) simulations. Species lifetimes in the cloud scenario are limited by photoionization following W. F. Huebner & J. Mukherjee (2015) and A. V. Oza et al. (2019). The exoplanet transit duration is given by $t_{1-4} = 2.8032 \pm 0.0192$ h (F. Faedi et al. 2011). 1D SERPENS cuts against observations representing minimum optically thin column densities are described in Figs 4(i) (Na), (ii) (K), and (iii) (SO_2).

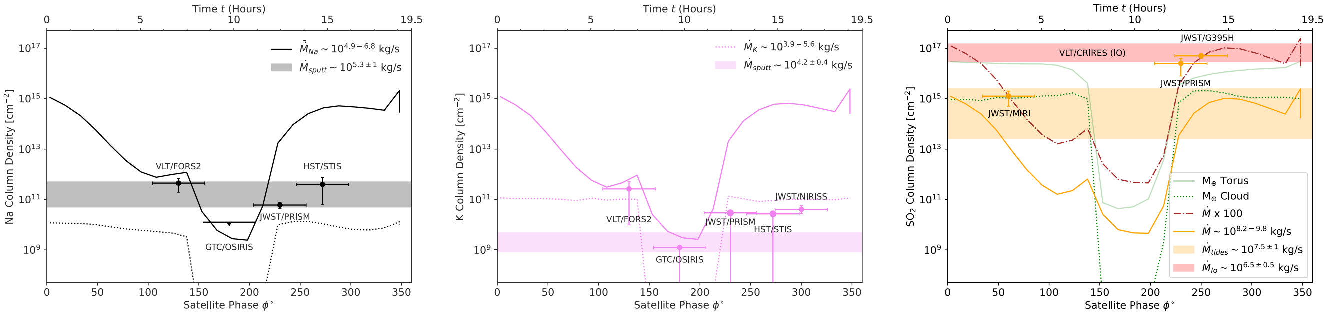

(i) Neutral Sodium (Na I) (ii) Neutral Potassium (K I) (iii) Neutral Sulfur Dioxide (SO_2)

Figure 4. Minimum LOS gas density variability of alkali metals and sulphur dioxide gas over several epochs. Data points: measurement from each instrument/epoch for Na (black), K (pink), and SO_2 (orange). X-errors: transit duration (2.8 h). Horizontal bands: 1D predictions from three-body tidal heating estimates by A. V. Oza et al. (2019) for Na (grey), K (pink), and SO_2 (orange), with Io's observed column by VLT/CRIRES (red). Black, pink, orange light curves: 3D Monte Carlo simulations (M. Meyer zu Westram, A. V. Oza & A. Galli 2024) modelling sputtered clouds (dotted) and toroidal (solid) geometries. Panel (iii): Green light curves: SO_2 simulations for an Earth-sized satellite cloud (dash–dot) and torus (solid). Brown dash–dot is ∼100 times Io torus scenario in orange.

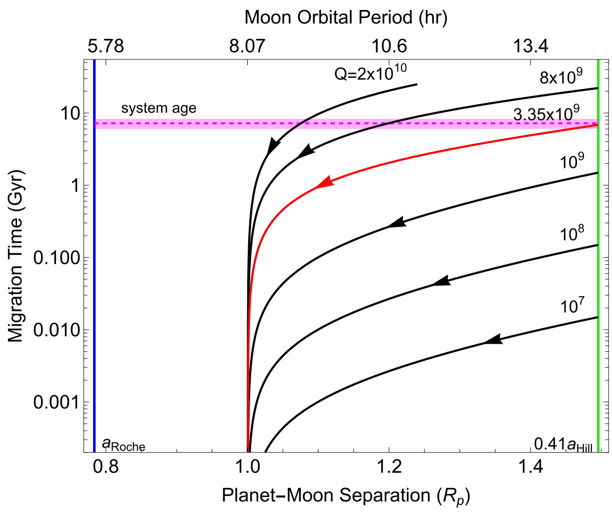

Figure 5. Moon migration plot for an exo-Io orbiting WASP-39 b. Each curve represents the time it takes for the moon to migrate due to equilibrium tides from a certain initial separation to the surface of the planet, for a given $\mathcal{Q}$ of the planet. The red curve pertains to the estimated $\mathcal{Q}$ of WASP-39 b based on the analysis in A. V. Oza et al. (2019). We assume the moon orbits faster than the planet spins, so that the moon falls towards the planet (towards the left of the plot). The pink region is the estimated age range of the system, at 7.2 Gyr. The vertical lines represent the Roche limit (blue) and Hill sphere (green).

is also considered in Fig. 4(iii). Through analysing the systems' evolution over time, we derive density *phase curves* that illustrate the average particle and LOS densities at any point in time over the duration of one exomoon's orbit. Results for Na limited by photoionization at higher velocities yield an elongated cloud reminiscent of the Io Banana cloud (W. H. Smyth & M. R. Combi 1988; J. K. Wilson et al. 2002) (see Fig. 3). Albeit, the exomoon cloud is more localized and lacks a complete toroidal structure due to short particle lifetimes. The online version of this paper provides a time-series sequence of Na evolution for both tori (Fig. 3a) and cloud (Fig. 3b) scenarios. The variations in average particle densities $\bar{n}$ primarily stem from radiative forces, resulting in minor fluctuations compared to the changes in average column densities $\bar{N}$. As lifetimes decrease further, particularly for K, evaporated material becomes increasingly confined to the exomoon, leading to a disappearance in the LOS signal during occultation. A prolonged species lifetime typically results in toroidal structures for small satellites. If the exomoon is massive the evaporated material may also return to the surface. These toroidal structures better distribute material along the orbit (similar to Io and Enceladus), which leads to less night-to-night variability while also increasing the total number of absorbing materials. This is particularly interesting for SO_2, where column densities are large and more consistent between the data retrievals. Our torus simulations of SO_2 in Fig. 3 suggest that column densities may vary by a significant amount but in a more controlled and continuous fashion. These trends are illustrated in Figs 4(i)–(iii) which show the temporal variability of integrated gas densities for Na, K, and SO_2 across different epochs and instruments as well as comparisons between simulated torus and cloud geometries under varying exomoon mass scenarios. We compute the maximum possible column density implied by a recent K I non-detection by Gran Telescopio Canarias/Optical System for Imaging and low Resolution Integrated Spectroscopy (C. Jiang et al. 2023) in Fig. 4(ii). In contrast, a confined SO_2 cloud, strictly limited to the photoionization lifetime, can cause a complete loss of signal during exomoon occultation – more akin to something we expect for K. Furthermore, integrating the column density of a photoionization limited SO_2 cloud over the transit duration does not yield large enough values to explain what we see in data. Whether it is reasonable to assume a prolonged lifetime of SO_2 molecules at WASP-39 b is difficult to assess. Although we do not explicitly track ions, which are known to influence the Jupiter-Io plasma torus (F. Bagenal 1994), we calculate photoionization and electron impact. The ionization rates imply a large presence of free electrons and SO_2 ions, which may boost the lifetime on the order of a transit duration.

4 CONCLUSIONS

Overall, we find that our numerical simulations in Fig. 4 are able to reproduce observed column densities, suggesting that a natural satellite source may not be negligible. For instance, especially for the Na and SO_2 cases in Figs 4(i) and (iii), a torus is required in comparison to cloud densities (dotted line) are far too small no matter the mass of the unknown satellite. For Na, an extended cloud, smaller than a torus, similar to the streams seen at Io approximates the epoch-to-epoch variability well. For K, since there is no identified KCl torus at Io, it may be possible that it is indeed a cloud, especially due to the disappearance of the K line completely in the *JWST*/PRISM data. Table 2's mass-loss ranges $\dot{M}$ indicate that an Na and K torus is, in principle, able to be sustained based on *JWST* and VLT data of evolving absorption features from subtle alkali absorption (sputtered cloud geometry) to large transit depths (torus geometry). The $\dot{M}_\gamma$–$\dot{M}_{\rm tor}$ values provide a range required to sustain N. Characterizing possible instrumental and stellar variability would benefit from dedicated repeat observations.

4.1 Volcanic exomoon output in time and mass flux

Results from the SERPENS simulations reveal that mass loss from an exomoon can produce strongly localized Na and K clouds. When integrating average Na column densities over the transit duration of ∼2.8 h, we are able to infer values comparable in magnitude to those in A. V. Oza et al. (2019). If K is locally bound to a putative exomoon, a natural explanation for a non-detection is the (partial) occultation of the satellite (and its exosphere) by the planet. Furthermore, as can be drawn from the phase curve in Fig. 4, a toroidal structure for SO_2 (green solid line) is better at explaining the subtly varying observational column densities while also providing large enough values when integrating over the transit duration. Sputtered clouds imply *orders* of magnitude variations, resulting in disappearances interpreted in Figs 4(i) and (ii) as alkali clouds, in contrast to the volcanic gas tori implying a more subtle variation between epochs ∼20. The behaviour is further consistent with PROMETHEUS geometries of an exomoon cloud and tori reported in Table 1 and Fig. 1.

The values inferred in Fig. 4 offer a range of possibilities for a putative exomoon to source the volcanic gases detected in transmission. By considering a cloud or toroidal lifetime τ_i as described in Section 2 following $\dot{M} \sim m N \pi R_\star^2/\tau_i$, we constrain roughly $\dot{M} \sim 10^{4.9-6.8}$, $10^{3.9-5.6}$, and $10^{8.2-9.8}$ kg s^{-1} for Na I (black), K I (pink), and SO_2 (orange), respectively, consistent with approximations predicted by A. V. Oza et al. (2019) (shaded regions) if a toroidal geometry is assumed (R. E. Johnson et al. 2006b; M. Meyer zu Westram 2023). The green phase curve of an Earth-mass satellite fits the data better than an Io-mass satellite (orange). Of course, it is also possible that a smaller satellite is interacting with the upper atmosphere of the gas giant, similar to Enceladus and Io, as the escape would be far larger (M. Meyer zu Westram et al. 2024). In that case, the mass-loss ranges may imply the putative satellite is in its last stage of evolution, on its way to transform into a ring satellite. Due to the favourable orbit of WASP-39 b, it may be that this satellite is still intact (Fig. 5), and has not yet fully disintegrated at the Roche limit (blue vertical line). The preferred tidal Q value from A. V. Oza et al. (2019), red line in Fig. 5, implies a migration time >10 Gyr to an orbit at the photosphere of ∼8.07 h, assuring the survival of the satellite. The red band indicated in Fig. 4 is the column density of Io, with the mass-loss range of volcanism needed to supply it against atmospheric sputtering (R. E. Johnson 2004). Hot Saturns in addition to WASP-39 b have now been modelled in 3D along with predictions of their NaD phase curves for HD 209458 b, HD 189733 b, WASP-49, WASP-96, WASP-69, WASP-17 b, XO-2N b, and HAT-P-1 b by M. Meyer zu Westram et al. (2024).

4.2 Outlook

Toroidal exosphere simulations from SERPENS and PROMETHEUS approximate an LOS column $N \sim 10^{16}$ SO_2 cm^{-2} from a tidally heated outgassing rate predicted in previous modelling at $\sim 10^{8.5}$ kg s^{-1}. Surprisingly this minimum rate for a toroidal geometry, changes by an order of magnitude for SO_2 as well, suggesting an exogenic process. The SO_2 column is nearly identical to Io's, whose disc is covered in IR-bright features near 4 μm (R. W. Carlson et al. 1997) and 7.3 μm as seen by ongoing *Juno*/Jovian Infrared Auroral Mapper (F. Tosi et al. 2020) and *JWST*/MIR observations (K. de Kleer et al. 2023). Evaluating Na/SO_2, the neutral observations vary from ∼2500 to 10 times less than Io's known $\chi_{\rm NaCl/SO_2}$ abundance (E. Lellouch et al. 2003), likely due to enhanced escape and heating beyond 1100 K. Interestingly, the Roche limit for a rock is interior to the planetary surface, therefore, atmosphere/exosphere interactions are especially important at this system. To constrain putative satellite orbits, high-resolution alkali Doppler shift observations are required (A. V. Oza et al. 2024; A. Unni et al. 2025). Since volcanic gas is expected to be accompanied by dust, recent *JWST* MIR observations are further suggestive of a natural satellite at this alkali hot Saturn system (L. Flagg et al. 2024) as well as other hot Jupiter systems studied in A. V. Oza et al. (2019) such as HD 189733 b (J. Inglis et al. 2024).

ACKNOWLEDGEMENTS

AVO thanks H. Knutson for valuable insight on *HST*/STIS and N. Nikolov on VLT/FORS2 data. The research described in this paper was carried out in part at the Jet Propulsion Laboratory, California Institute of Technology, under a contract with the National Aeronautics and Space Administration. Copyright 2025. All rights reserved. YM acknowledges support from the European Research Council (ERC) under the European Union's Horizon 2020 Framework Programme (grant agreement no. 101088557, N-GINE).

DATA AVAILABILITY

Relevant *JWST* data used in this study can be accessed through the Space Telescope Science Institute (STScI) archive at https://archive.stsci.edu.

REFERENCES

Ahrer E.-M. et al., 2023, Nature, 614, 653
Alderson L. et al., 2023, Nature, 614, 664
Ashton E., Gladman B., Alexandersen M., Petit J.-M., 2025, Res. Notes Am. Astron. Soc., 9, 57
Bagenal F., 1994, J. Geophys. Res., 99, 11043
Bello-Arufe A. et al., 2025, ApJ, 980, L26
Carlson R. W. et al., 1997, Geophys. Res. Lett., 24, 2479
Cassidy T. A., Mendez R., Arras P., Johnson R. E., Skrutskie M. F., 2009, ApJ, 704, 1341
Charnoz S., Canup R. M., Crida A., Dones L., 2018, in Tiscareno M. S., Murray C. D., eds, Planetary Ring Systems: Properties, Structure, and Evolution. Cambridge Univ. Press, Cambridge, p. 517
de Kleer K. et al., 2023, JWST Proposal. Cycle 2, ID #4078
Draine B. T., 2011, Physics of the Interstellar and Intergalactic Medium. Princeton Univ. Press, Princeton, NJ
Faedi F. et al., 2011, A&A, 531, A40
Fegley B., Zolotov M. Y., 2000, Icarus, 148, 193
Feinstein A. D. et al., 2023, Nature, 614, 670
Fischer P. D. et al., 2016, ApJ, 827, 19
Flagg L. et al., 2024, ApJ, 969, L19
Foreman-Mackey D., Hogg D. W., Lang D., Goodman J., 2013, PASP, 125, 306
Fournier-Tondreau M. et al., 2025, MNRAS, 539, 422
Gebek A., Oza A. V., 2020, MNRAS, 497, 5271
Gibson N. P., de Mooij E. J. W., Evans T. M., Merritt S., Nikolov N., Sing D. K., Watson C., 2019, MNRAS, 482, 606

Herrick R. R., Hensley S., 2023, Science, 379, 1205
Huebner W. F., Mukherjee J., 2015, Planet. Space Sci., 106, 11
Inglis J. et al., 2024, ApJ, 973, L41
Jiang C., Chen G., Pallé E., Murgas F., Parviainen H., Ma Y., 2023, A&A, 675, A62
Johnson R. E., 2004, ApJ, 609, L99
Johnson R. E., Huggins P. J., 2006, PASP, 118, 1136
Johnson R. E., Strobel D. F., 1982, J. Geophys. Res., 87, 10385
Johnson R. E. et al., 2006a, Icarus, 180, 393
Johnson R. E., Smith H. T., Tucker O. J., Liu M., Burger M. H., Sittler E. C., Tokar R. L., 2006b, ApJ, 644, L137
Kisare A. M., Fabrycky D. C., 2024, MNRAS, 527, 4371
Kleisioti E., Dirkx D., Rovira-Navarro M., Kenworthy M. A., 2023, A&A, 675, A57
Kleisioti E., Dirkx D., Tan X., Kenworthy M. A., 2024, A&A, 687, A125
Lellouch E., Paubert G., Moses J. I., Schneider N. M., Strobel D. F., 2003, Nature, 421, 45
Lellouch E., Ali-Dib M., Jessup K.-L., Smette A., Käufl H.-U., Marchis F., 2015, Icarus, 253, 99
Mahieux A. et al., 2023, Icarus, 399, 115556
Meyer zu Westram M., 2023, SERPENS – Simulating the Evolution of Ring Particles Emergent from Natural Satellites. Available at: https://github.com/momzw/SERPENS
Meyer zu Westram M., Oza A. V., Galli A., 2024, J. Geophys. Res.: Planets, 129, e2023JE007935
Narang M., Oza A. V., Hakim K., Manoj P., Banyal R. K., Thorngren D. P., 2023a, AJ, 165, 1
Narang M. et al., 2023b, MNRAS, 522, 1662
Nikolov N., Sing D. K., Gibson N. P., Fortney J. J., Evans T. M., Barstow J. K., Kataria T., Wilson P. A., 2016, ApJ, 832, 191
Oza A. V. et al., 2019, ApJ, 885, 168
Oza A. V. et al., 2024, ApJ, 973, L53
Patel J. A. et al., 2024, A&A, 690, A159
Peale S. J., Cassen P., Reynolds R. T., 1979, Science, 203, 892
Powell D. et al., 2024, Nature, 626, 979
Quick L. C., Roberge A., Mlinar A. B., Hedman M. M., 2020, PASP, 132, 084402
Reif F., 1965, Fundamentals of Statistical and Thermal Physics. McGraw-Hill, New York
Rustamkulov Z. et al., 2023, Nature, 614, 659
Schmidt C. et al., 2023, Planet. Sci. J., 4, 36
Sheppard S. S. et al., 2018, Res. Notes Am. Astron. Soc., 2, 155
Sheppard S. S., Tholen D. J., Alexandersen M., Trujillo C. A., 2023, Res. Notes Am. Astron. Soc., 7, 100
Sing D. K. et al., 2016, Nature, 529, 59
Smyth W. H., Combi M. R., 1988, ApJ, 328, 888
Sulcanese D., Mitri G., Mastrogiuseppe M., 2024, Nat. Astron., 8, 973
Tennyson J. et al., 2024, J. Quant. Spectrosc. Radiat. Transf., 326, 109083
Tokadjian A., Piro A. L., 2023, AJ, 165, 173
Tosi F. et al., 2020, J. Geophys. Res.: Planets, 125, e06522
Tsai S.-M. et al., 2023, Nature, 617, 483
Unni A. et al., 2025, MNRAS, 540, L48
Veeder G. J., Matson D. L., Johnson T. V., Blaney D. L., Goguen J. D., 1994, J. Geophys. Res., 99, 17095
Wakeford H. R. et al., 2018, AJ, 155, 29
Wilson J. K., Mendillo M., Baumgardner J., Schneider N. M., Trauger J. T., Flynn B., 2002, Icarus, 157, 476
Yang J., Hu R., 2024, ApJ, 966, 189
Yung Y. L., DeMore W. B., 1999, Photochemistry of Planetary Atmospheres. Oxford Univ. Press, Oxford

This paper has been typeset from a TEX/LATEX file prepared by the author.